J. Micromech. Microeng. **23** (2013) 025005 (9pp) doi:10.1088/0960-1317/23/2/025005

Integration of BST varactors with surface acoustic wave device by film transfer technology for tunable RF filters

Hideki Hirano[1], Tetsuya Kimura[2], Ivoyl P Koutsaroff[2], Michio Kadota[2], Ken-ya Hashimoto[3], Masayoshi Esashi[4] and Shuji Tanaka[1]

[1] Graduate School of Engineering, Tohoku University, Sendai, Japan
[2] Murata Manufacturing Co. Ltd, Nagaokakyo, Kyoto, Japan
[3] Graduate School of Engineering, Chiba University, Chiba, Japan
[4] Advanced Institute for Material Research, Tohoku University, Sendai, Japan

E-mail: hirano@mems.mech.tohoku.ac.jp

Received 4 October 2012, in final form 17 November 2012
Published 21 December 2012
Online at stacks.iop.org/JMM/23/025005

Abstract
This paper presents a film transfer process to integrate barium strontium titanate (BST) metal–insulator–metal (MIM) structures with surface acoustic wave (SAW) devices on a lithium niobate (LN) substrate. A high-quality BST film grown on a Si substrate above 650 °C was patterned into the MIM structures, and transferred to a LN substrate below 130 °C by Ar-plasma-activated Au–Au bonding and the Si lost wafer process. Simple test SAW devices with the transferred BST variable capacitors (VCs) were fabricated and characterized. The resonance frequency of a one-port SAW resonator with the VC connected in series changed from 999 to 1018 MHz, when a dc bias voltage of 3 V was applied to the VC. Although the observed frequency tuning range was smaller than expected due to the degradation of BST in the process, the experimental result demonstrated that a tunable SAW filter with the transferred BST VCs was feasible.

(Some figures may appear in colour only in the online journal)

1. Introduction

Since wireless communication is becoming more heavily used to send a large amount of rich content, advanced mobile phones are required to support a variety of wireless services at different frequency bands. As a result, a modern mobile phone has a quite complicated wireless front-end, which is composed of many filters, amplifiers, mixers etc. To make a wireless system simpler and even flexible, a reconfigurable wireless front-end is expected. Furthermore, a cognitive radio, which automatically changes to the best frequency based on spectrum sensing, is under development to solve frequency resource shortage problems [1, 2]. Wide frequency range tunable radio-frequency (RF) bandpass filters with low insertion loss, sharp cut-off characteristics and small size are urgently required for such advanced wireless systems.

RF filters based on surface acoustic wave (SAW) and bulk acoustic wave (BAW) resonators have been widely used in mobile communications because of their excellent features such as small size, low insertion loss and sharp cut-off characteristics. However, wide frequency tuning of such acoustic wave resonators is difficult, because the resonance frequency of SAW and BAW devices is basically determined by their dimensions (e.g. interdigital transducer (IDT) pitch and film/plate thickness) and acoustic velocity, both of which are difficult to change widely. Recently, a ladder-type tunable RF filter using SAW/BAW resonators with variable capacitors (VCs) connected in parallel and/or series has been proposed [3]. Both passband width and center frequency can be flexibly controlled by applying a dc bias voltage to the VCs. Based on this concept, we developed the tunable filter where SAW resonators and electrostatically-actuated microelectromechanical systems (MEMS) VCs were integrated on lithium niobate (LN) [4]. The 3 dB bandwidth was tuned from 146 to 130 MHz by actuating the MEMS VC connected in parallel to one of the series resonators.

In the previous study, we selected the MEMS VCs, because they can be directly fabricated on a SAW device substrate by photolithography and electroplating. A high Q factor and good linearity of an air-gap VC are also important for this application. However, the relatively large size of the MEMS VCs in comparison with the SAW resonators is a problem for consumer applications. On the other hand, the footprint of a VC made of ferroelectric materials such as barium strontium titanate (BST) is several hundredths smaller than that of the air-gap VC due to its dielectric constant as high as several hundreds. For example, the footprint of a 200 nm thick BST VC with the maximum capacitance of 2.1 pF is 25 μm square, while a MEMS VC with 0.5 μm air gap occupies 700 μm $\times$ 600 μm in area.

It has other advantages, including a high tuning ratio with low control voltage and good linearity at the GHz range [5, 6]. The dielectric constant of BST is tuned by an applied dc electric field, and tunability greater than several hundred per cent is achievable [7]. By varying the film thickness, the operating voltage can be widely designed, depending of the application.

From the above characteristics, BST has shown great promise for tunable RF and microwave components, such as voltage-controlled oscillators, tunable filters and phase shifters [8–10]. However, the deposition of a high-quality BST film on a SAW device substrate such as LN and lithium tantalate (LT) has not been demonstrated, because it needs high temperature (>600 °C) to obtain large tunability in dielectric constant [11]. The high temperature deposition may cause thermal damages to a BST film due to difference in the coefficient of thermal expansion (CTE) between the BST film and a LN or LT substrate. In addition, LT and LN can be damaged, when they are heated at such a high temperature. This is partly because the crystal surface accumulates electric charges causing spontaneous electrical discharge, when pyroelectric LT and LN are heated [12]. Another reason is a change in the chemical composition, which is more severe for LT than LN.

To integrate the functional film which is difficult to deposit directly onto a different material of substrate, a film transfer process is useful. For example, Al–As–Ga-based LED elements epitaxially grown on a GaAs substrate were transferred and integrated with a Si-based IC drivers by sacrificially layer etching technique [13]. Electroplated Ni microstructures grown on a donor wafer were transferred to a target wafer using a weakly adhesive sublayer between the Ni microstructures and the donor wafer [14]. Polycrystalline silicon infrared bolometers grown on a silicon substrate were transferred to a Si-based IC by sacrificial wafer etching [15]. AFM cantilevers were transferred selectively to many wafers using an adhesive polymer layer and device release based on laser ablation [16]. Single crystal $LiNbO_3$ wafers were transferred to a Si substrate by room-temperature Au–Au bonding for thin film ridge waveguides [17] and bulk acoustic resonator [18].

In this study, we have developed a ferroelectric film transfer process to integrate BST VCs with SAW devices at low temperature for tunable RF filter application. High-quality BST films grown on a Si substrate were transferred onto a 15° Y $LiNbO_3$ wafer by the Si lost wafer process. In section 2, the principle of a tunable SAW filter using additional VCs is explained, and the design of a test device with BST VCs is described. In section 3, the outline of our experiments on the BST transferring process is shown. Finally, fabrication results, the evaluation of transferred BST VCs and the characterization of test SAW devices with BST VCs are described in section 4.

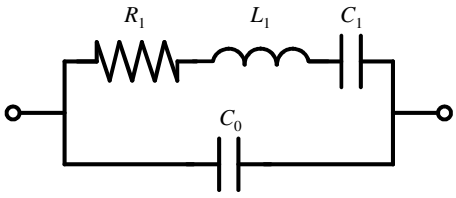

Figure 1. Electrical equivalent circuit of an acoustic resonator.

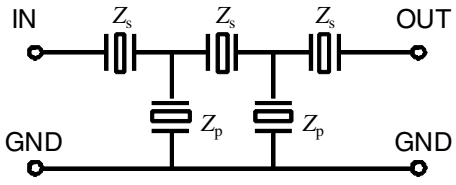

Figure 2. Basic configuration of the ladder-type SAW filter.

2. Principle and design

2.1. Principle

Figure 1 shows the equivalent circuit of an acoustic resonator, where L_1, R_1 and C_1 are referred as motional inductance, motional resistance and motional capacitance, respectively, while C_0 is the electrical shunt capacitance. The circuit impedance takes the minimum at a frequency f_r called the resonance frequency, which is given by

$$f_r = 1/2\pi\sqrt{L_1C_1}. \tag{1}$$

It takes the maximum at a frequency f_a called the anti-resonance frequency, which is given by

$$f_a = 1/2\pi\sqrt{L_1(C_1^{-1} + C_0^{-1})^{-1}} \tag{2}$$

Figure 2 shows the configuration of the conventional ladder-type filter, which is composed of two types of resonator Z_s and Z_p placed in series and parallel arms, respectively. Here, the resonance frequency f_r^s of the series element Z_s is identical to the anti-resonance frequency f_a^p of the parallel element Z_p. Efficient signal transfer is possible through the filter at a frequency f_c ($= f_r^s = f_a^p$), while the signal transfer is rejected at f_a^s and f_r^p. Thus, the filter exhibits a typical bandpass characteristic shown in figure 3.

Consider the configuration where a capacitor C is connected to a SAW resonator in parallel as shown in figure 4(*a*). When the quality factor Q of the resonator is sufficiently high, the simple LCR model shows that the anti-resonant frequency decreases according to

$$f_a^e = f_a\sqrt{1 - \frac{1}{\gamma + 1}\cdot\frac{C}{C_0 + C}}, \tag{3}$$

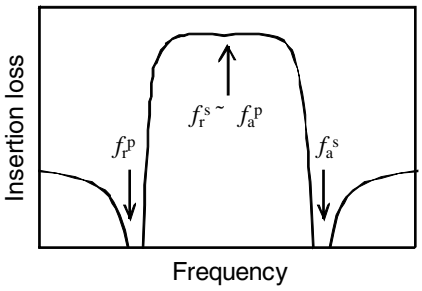

Figure 3. Typical transmission characteristics of the ladder-type SAW filter.

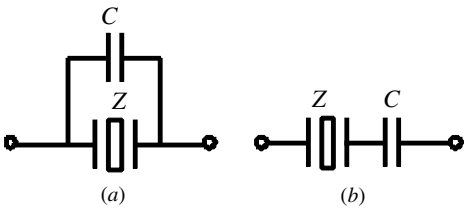

Figure 4. Capacitor, C, connected (a) in parallel and (b) in series to a SAW resonator, Z.

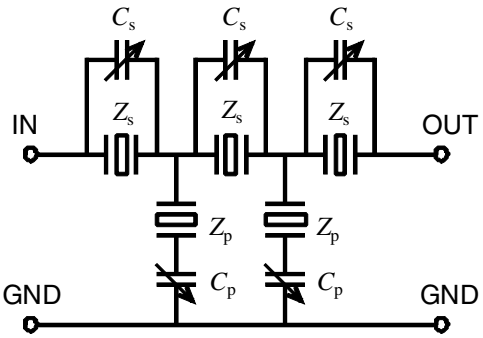

Figure 5. Circuit diagram of a tunable filter consisting of variable capacitor, C, and SAW resonator, Z.

while the resonance frequency does not change. In equation (3), γ is capacitance ratio C_0/C_1, which is roughly inversely proportional to the electromechanical coupling coefficient (k^2). On the other hand, when a capacitor C is connected to a resonator in series as shown in figure 4(b), the resonant frequency increases according to

$$f_r^e = f_r\sqrt{1+\frac{1}{\gamma}\cdot\frac{C_0}{C_0+C}}, \tag{4}$$

while the anti-resonance frequency does not change. Therefore, the positions of $f_a{}^s$ and $f_r{}^p$ shift inside when additional capacitances are connected in series with Z_p, and in parallel with Z_s, as shown in figure 5. Figure 6 shows typical transmission characteristics of a ladder-type SAW filter without additional VCs (solid line), with VCs in series and in parallel showing the minimum capacitance (dotted line), and with VCs in series and in parallel showing the maximum capacitance (dashed line). When the capacitances of the VCs are adjusted, the upper and lower passband edges can be tuned independently within the arrowed region as shown in figure 6. Therefore, the bandwidth and the center frequency can be tuned by changing the capacitance of the additional VCs. In

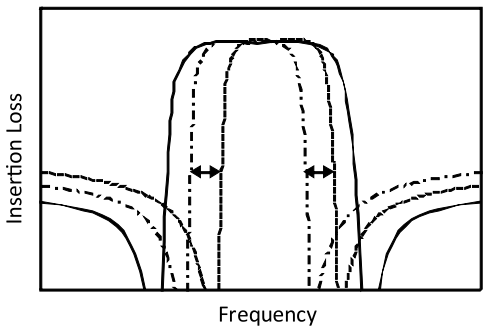

Figure 6. Transmission characteristics of a ladder type SAW filter without additional VCs (solid line), with VCs in series and in parallel showing the minimum capacitance (dotted line), with VCs in series and in parallel showing the maximum capacitance (dashed line).

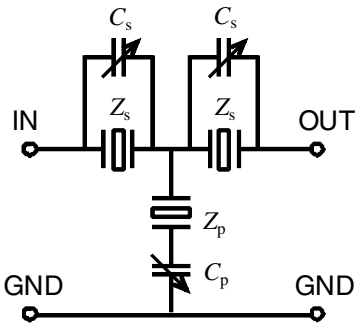

Figure 7. Configuration of a test SAW device.

order to obtain widely-tunable filters, the VCs must have large tunability in capacitance. Wider frequency tunability can be realized using the filter configuration where two capacitors C_s and C_p are connected to each resonator in series and in parallel, respectively. The device configuration and tuning capability are described elsewhere more in detail [3].

2.2. Device design

Based on the above principle, the frequency tuning range is absolutely limited within the original bandwidth of the filter without additional capacitors. Therefore, a wideband filter, which is composed of high k^2 resonators, is necessary to obtain practical frequency tunability. In this study, we have adopted the Love wave, which is a kind of SAW with an extremely high k^2 ($\sim 30\%$), for the resonators. A Love wave can be generated on a lightly-rotated Y-cut LN substrate with heavy (e.g., thick Cu and Au) IDT electrodes [19].

For the proof of concept, a simple T-type resonator configuration with VCs, as shown in figure 7, was selected as a test device. A test device with a center frequency of 1.12 GHz was designed, assuming that the dielectric constant of a BST film decreased to one third of the initial value with dc bias voltage. The design is summarized in table 1. From equations (3) and (4), the center frequency moves from 1.088 to 1.127 GHz, i.e. the expected frequency tunability is 3.6%.

3. Experimental methods

3.1. Fabrication process

In this study, diced 20 mm square Si and LN substrates were used for fabricating the test device. The fabrication process is shown in figure 8. First, IDT electrodes of Au/Ti for the Love wave were fabricated on a 15° Y LN substrate by electron beam lithography (figure 8(*a*)), and wiring lines and bonding pads of Au/Ti were fabricated by the lift-off process (figure 8(*b*)). The thickness of the Au/Ti layer for the IDT electrodes and the bonding pads is 100 nm/8 nm and 200 nm/8 nm, respectively.

For the deposition of BST, the double-sided polished Si wafer of 200 μm in thickness was thermally oxidized. On it, 20 nm thick TiO_2, 100 nm thick Pt and 200 nm thick BST were deposited in this order by sputtering. The deposition temperature of BST was 650 °C. The BST and Pt layers were patterned by HF + HNO_3 wet etching and Xe ion etching, respectively (figure 8(*c*)). On the patterned BST, 100 nm thick Au pads for bonding were formed by the lift-off process, and the backside oxide layer was patterned into alignment marks for wafer-to-wafer bonding using buffered HF (figure 8(*d*)). Before the bonding, the bonding surfaces on both Au/BST/Pt metal–insulator–metal (MIM) structures on the Si substrate and the Au bonding pads on the LN substrate were activated by Ar plasma for 1 min to enhance adhesion between the bonding pads [20].

Au–Au bonding was performed within 60 min after the Ar plasma activation, because the surface was gradually deactivated in air. The BST MIM structures on the Si substrate were aligned and bonded to the Au pads on the LN substrate by applying a pressure of 3 MPa at 100–150 °C for 20 min in vacuum (figure 8(*e*)). After bonding the LN and Si substrates, all of the Si bulk layer of 200 μm thick was etched off by a SF_6 plasma (figure 8(*f*)), and the oxide layer was removed by buffered HF etching (figure 8(*g*)). Finally, the BST MIM structures were covered with a photo-patternable polyimide insulating layer with wiring apertures, and then Al wirings were formed for connecting the BST VCs and the SAW resonators (figure 8(*h*)).

3.2. Evaluation method

The capacitance of the BST MIM structures was measured before and after the film transfer process using a HP 4284A LCR meter. The fabricated test devices were characterized using an Agilent 5071B network analyzer, Cascade SG/GS-250 RF wafer probes and a modified probe for dc voltage application.

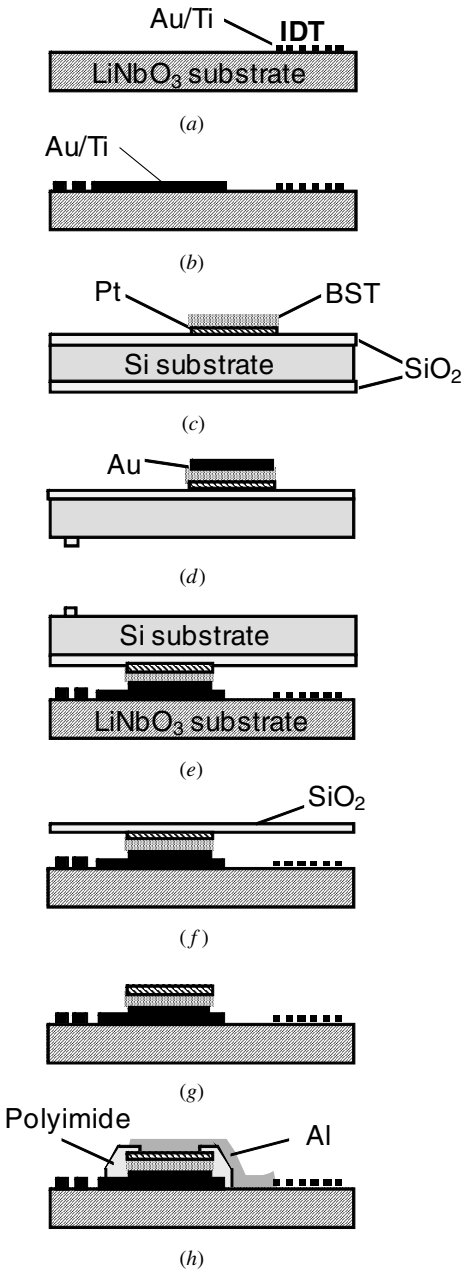

Figure 8. Fabrication process of the tunable filter using the BST transfer technique. (*a*) IDT fabrication by EB lithography, (*b*) bonding pads fabrication by lift-off, (*c*) deposition and patterning of Pt and BST on Si, (*d*) deposition of Au on BST using the lift-off process and backside alignment mark fabrication, (*e*) bonding Si wafer to LN wafer, (*f*) etch-off of Si substrate by the SF_6 plasma process, (*g*) etching of SiO_2 layer, and (*h*) polyimide insulation and wiring between IDT and VCs.

Table 1. Design of tunable filter using VCs.

	Center frequency (MHz)	Lower rejection (MHz)	Upper rejection (MHz)
Without additional capacitance	1122	987	1256
Initial capacitance (6pF)	1088	1036	1141
Decreased capacitance (2pF)	1127	1073	1181

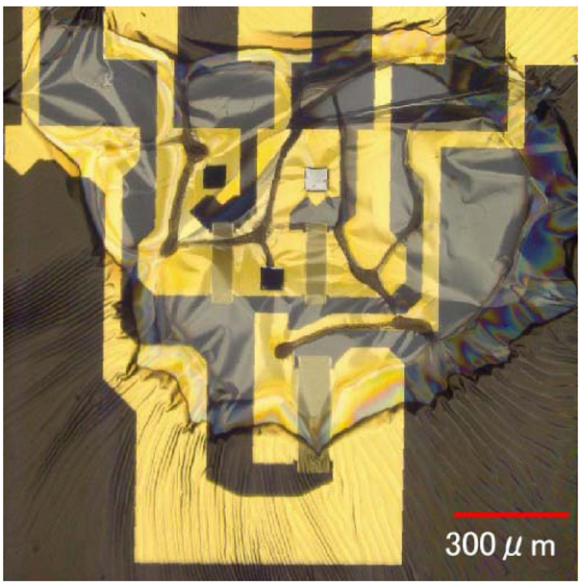

Figure 9. Optical micrograph of a wrinkled SiO_2 film after a Si substrate was etched off.

4. Results and discussion

4.1. Fabrication result

When the Si wafer was bonded to the LN substrate at 150 °C, the bonded substrates separated automatically at the BST/Pt or Pt/TiO_2 interface during cooling, while no separation was observed at bonding temperatures less than 130 °C. A large mismatch in CTE between Si (CTE: 2.6 × 10^{-6} K^{-1}) and LN (CTE: 14.4 × 10^{-6} K^{-1} for a axis and 7.5 × 10^{-6} K^{-1} for *c* axis) [21] might cause the separation, when the bonding temperature was above 150 °C.

After Si substrate removal by a SF_6 plasma, the SiO_2 film as a barrier layer was wrinkled as shown in figure 9, and thus a part of the BST MIM structure was pulled by the SiO_2 film and peeled from the LN substrate at the Au–Au interface, as shown in figure 10(*a*). This wrinkling phenomenon was caused by residual internal stress of the SiO_2. Some BST MIM structures near the wafer edge were successfully transferred to the LN substrate, although the SiO_2 film surrounding the BST was curled as shown in figure 10(*b*). If the Au–Au bonding strength is higher than the internal stress of the SiO_2, the BST MIM structures can be transferred to the LN substrate. Uneven distribution of the transferred BST group indicates that the local Au–Au bonding failure was caused by particulate contamination on the bonding surfaces. Since most particles were generated from the dicing edge of the Si and LN substrates, the use of a full wafer without dicing and intensive wafer cleaning can improve the film transferring yield.

Figure 11 shows the SEM image of the transferred BST MIM structures. No visible damage was observed on the surface, however, partial peeling, which might be also caused by the stress of the SiO_2 film, was found at the edge of the MIM structures. Figure 12 shows the optical micrograph and schematic cross section of the completed test device.

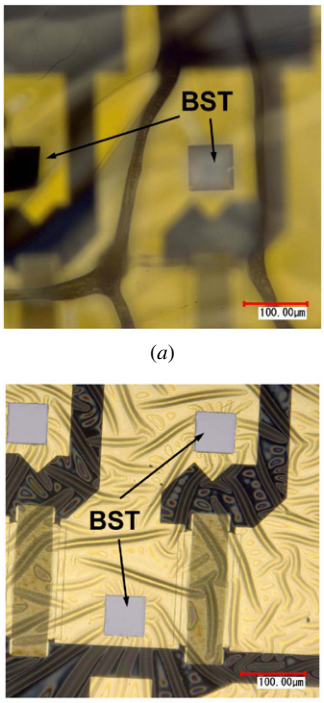

Figure 10. Optical micrograph of BST structures and the winkled SiO_2 film. (*a*) BST peeled at the Au/Au interface. (*b*) Transferred BST on LN wafer.

4.2. Evaluation of BST varactor

The dielectric constant of BST as a function of dc bias voltage was measured just after deposition and after transfer, as shown in figures 13(*a*) and (*b*), respectively. The dielectric constant of BST just after deposition was initially 800 and was changed to 200 with the application of 8 V. The tangent δ of the VCs was less than 0.02 at any voltage. As shown in figure 13(*b*), the transferred BST worked as a VC, however, the dielectric constant of the transferred BST became approximately a half of the original value. As discussed in [22], trapped charges by penetrated positive ions from plasma to the BST films might cause the reduction of the dielectric constant during the plasma etching process of BST and Pt. The dielectric constant can be recovered by annealing at 600 °C in oxygen ambience after etching, due to the release of the trapped charges. The insertion of a thin plasma-damaged photoresist residue layer with low dielectric constant between BST and Au can also reduce the apparent dielectric constant.

Figure 14 shows the optical micrograph of the BST VC before and after applying a dc bias voltage of 4 V. Damage due to a short circuit was visually found after applying the dc bias voltage. The leak path might be caused by the Pt debris which was redeposited on the MIM sidewalls during the ion etching of the Pt layer [23]. Pt etching using Cl-based plasma reduces Pt redeposition on the sidewalls [24], however, Cl plasma also reduces the dielectric constant of a BST film due to the formation of a metal (Ba or Sr) chloride compound layer on the BST surface during Cl-based plasma etching [25]. This problem can be solved by CO/NH_3 reactive ion etching for Pt patterning [26].

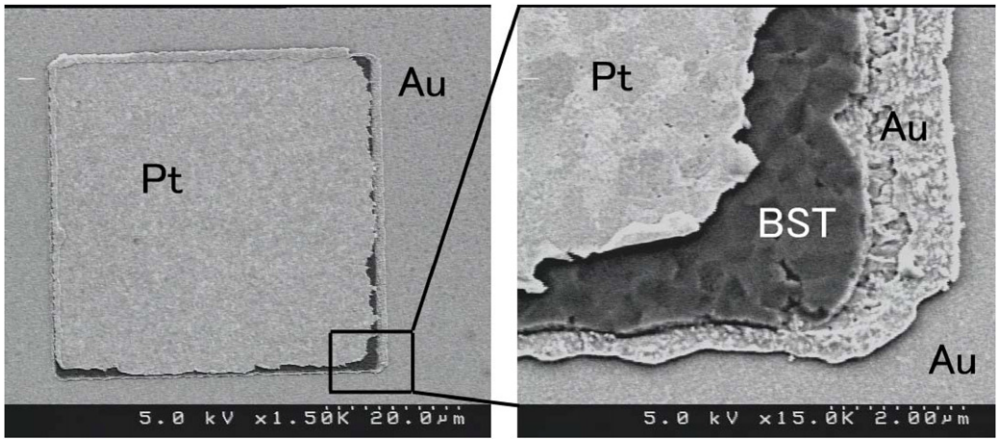

Figure 11. SEM image of the transferred BST MIM structures on a LN wafer.

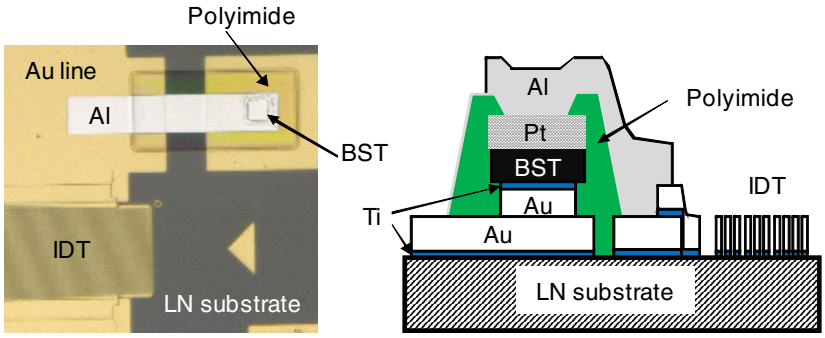

(*a*) (*b*)

Figure 12. (*a*) Optical micrograph and (*b*) schematic cross section of the integrated BST VC with a SAW resonator.

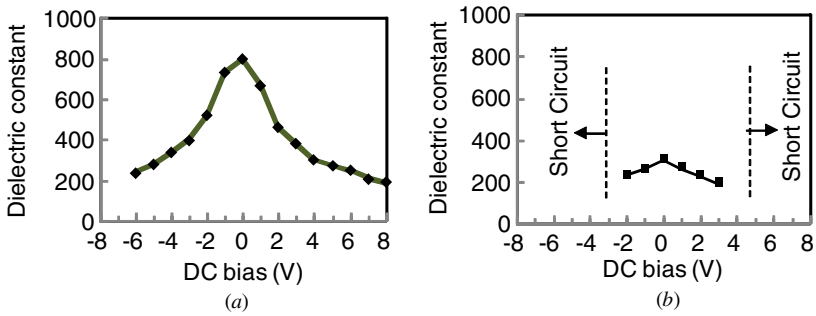

(*a*) (*b*)

Figure 13. Dielectric constant of BST films as a function of dc bias voltage: (*a*) As-deposited BST on a Si wafer, (*b*) transferred BST on a LN wafer.

4.3. Characterization of test device

Figures 15(*a*) and (*b*) show the optical micrograph of the T-type resonator configuration without and with the VCs, respectively. Both of them have the same IDT design and were fabricated on the same LN substrate. The test device worked as a simple filter, and the 3 dB bandwidth and the center frequency were 280 MHz and 1.197 GHz, respectively, without the VCs, as shown in figure 16. By connecting the VCs to the IDT, on the other hand, the 3 dB bandwidth was narrowed to 197 MHz, while the center frequency (1.193 GHz) was scarcely changed. The insertion losses of the filter without and with inserting VCs are almost the same, 1.56 and 1.31 dB, respectively. The S-parameter simulation shows that the insertion loss is not influenced by the capacitance but by the Q factor of the VCs [3]. Because the Q factor of BST (∼50) is high enough for this application, the increase of insertion loss by the inserted capacitance may be negligible. Failure in the transfer of C_{S1} caused the splitting of the upper rejection pole, because the original rejection pole of Z_{S1} without C_{S1} and the sifted rejection pole of Z_{S2} with C_{S2} were separated.

The capacitance of the transferred BST capacitor without applying dc bias voltage was calculated as 3.06 pF based on the size and dielectric constant. The original resonance and anti-resonance frequencies, i.e. lower and upper rejection poles without connecting the VCs, was 1000 and 1399 MHz, respectively. The theoretical change in the resonance and anti-resonance frequency by connecting the additional BST capacitor was calculated using equations (3) and (4), assuming

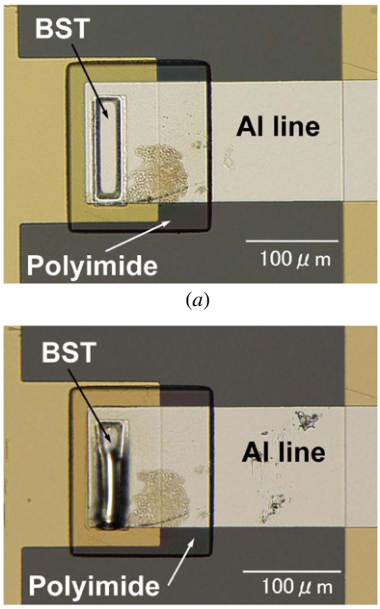

Figure 14. Transferred BST VCs on a LN wafer (*a*) before applying voltage and (*b*) after applying 6 V.

Table 2. Characteristics of filter with VCs.

	Center frequency (MHz)	Lower rejection (MHz)	Upper rejection (MHz)
Measurement	1193	1078	1310
Calculation	1193	1072	1314

that C_0^s, C_0^p and γ were 2.0, 3.0 pF and 3.3 pF, respectively. Table 2 compares the calculated and measured results in terms of the center frequency and the upper and lower rejection poles. Both results show reasonable agreement, demonstrating that a tunable SAW filter is feasible by using the BST film transfer process.

4.4. Frequency tuning by BST variable capacitor

Figure 17 shows the optical micrograph of a one-port SAW resonator with the transferred BST VC connected in series. Frequency tuning by the VC was simply demonstrated using this test device. Figure 18 shows the imaginary part of S_{11} ($Im(S_{11})$) with and without applying a dc bias voltage to the VC. The lower and upper zero-cross points of $Im(S_{11})$ correspond to resonance and anti-resonance frequencies, respectively. By applying 3 V to the VC, the resonance frequency moved from 999 to 1018 MHz, while the anti-resonance frequency did not move, as the theory presented in section 2 indicates. However, the amount of frequency shift was not as large as expected. If the VC has a dielectric constant tunability of 300%, the frequency shit should be 37 MHz, which is twice the experimental result. This can be attributed to the degradation of the VC, as mentioned above.

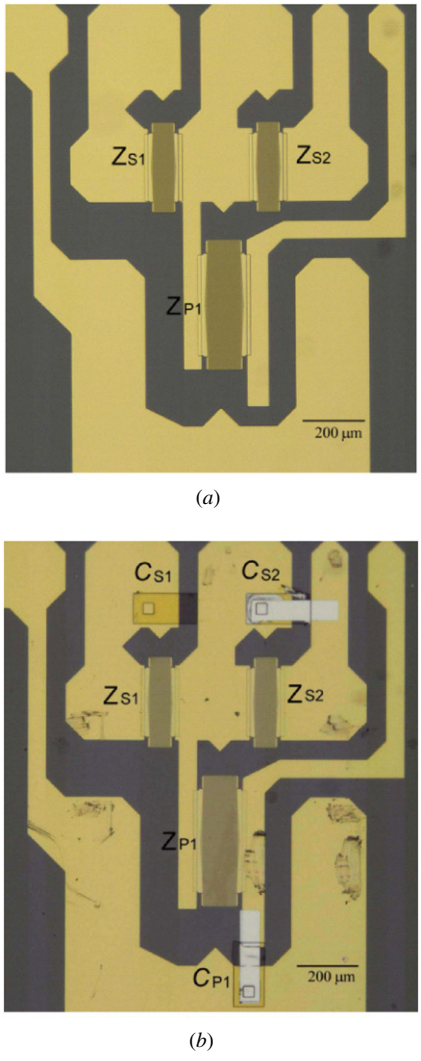

Figure 15. T-type SAW filter configuration (*a*) without BST VCs, (*b*) with BST VCs. C_{s1} is open due to the failure of BST transfer.

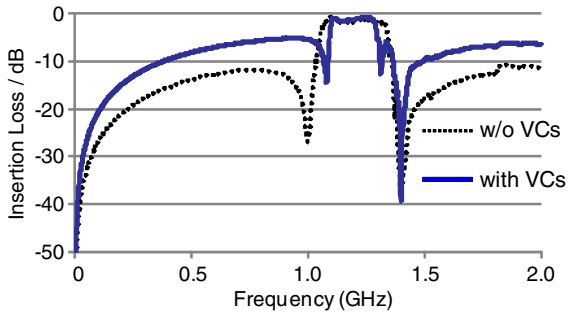

Figure 16. Filter response of the T-type SAW filter without BST VCs (dotted line) and with BST VCs (solid line).

5. Conclusion

We developed a BST film transfer technology for tunable RF bandpass filters consisting of SAW resonators and BST variable capacitors (VCs). BST was deposited on a Si substrate at 650 °C, patterned into metal–insulator–metal structures, and then transferred to a lithium niobate substrate. The transfer process consisted of low temperature Au–Au bonding after Ar

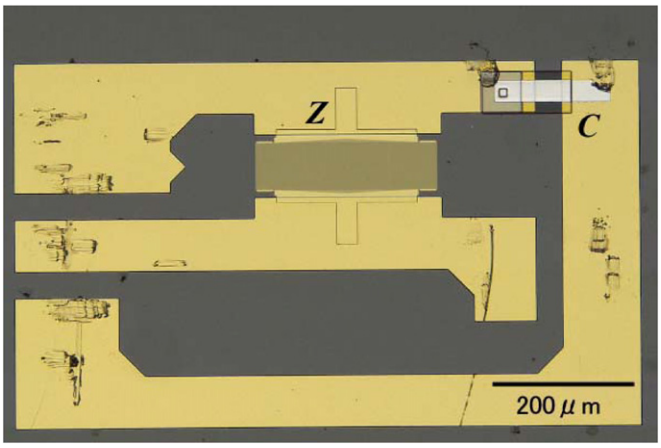

Figure 17. Optical micrograph of the 1-port SAW resonator with VCs in series.

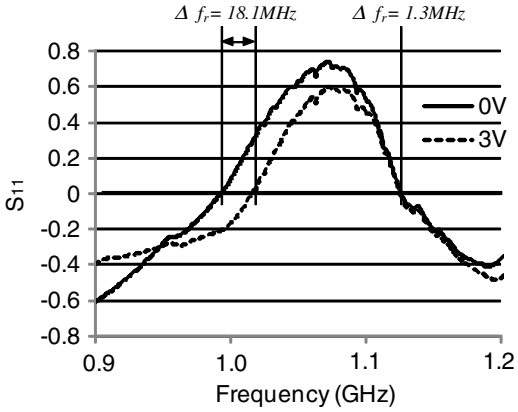

Figure 18. Imaginary part of S_{11} of the 1-port SAW resonator with BST VCs in series. The solid line represents no bias voltage and the dotted line a 3 V bias voltage.

plasma activation and a Si lost wafer process by SF_6 plasma. The resonance frequency of a one-port SAW resonator with the transferred BST VC connected in series increased from 999 to 1018 MHz, when a dc bias voltage of 3 V was applied to the VC. This is clear evidence that the frequency tuning of a SAW filter is possible using the transferred BST VCs. Problems left in this study are the insufficient yield of the transfer process and the degradation of BST due to process damage. After solving these problems, the film transfer process can be applied to not only tunable SAW filters with BST VCs but also used in other applications using functional thin-film materials, e.g. tunable BAW devices and integrated optical devices.

Acknowledgment

This research was supported by the Japan Society for the Promotion of Science (JSPS) through its 'Funding Program for World-Leading Innovative R&D on Science and Technology (FIRST Program).'

References

[1] Harada H 2008 A small-size software defined cognitive radio prototype *PIMRC'08: Proc. IEEE 19th Int. Symp. Personel, Indoor and Mobile Radio Commun. (Cannes, France)*

[2] Abidi A A 2007 The path to the software-defined radio receiver *IEEE J. Solid-State Circuits* **42** 954–66

[3] Komatsu T, Hashimoto K, Omori T and Yamaguchi M 2010 Tunable radio-frequency filters using acoustic wave resonators and variable capacitors *Japan. J. Appl. Phys.* **49** 07HD24

[4] Yasue T, Komatsu T, Nakamura N, Hashimoto K, Hirano H, Esashi M and Tanaka S 2012 Wideband tunable Love wave filter using electrostatically-actuated MEMS variable capacitors integrated on lithium niobate *Sensors Actuators* A **188** 456–62

[5] Zhu X, Zhu J, Zhou S, Liu Z, Ming N, Lu S, Chan H L and Choy C L 2003 Recent progress of (Ba,Sr)TiO_3 thin films for tunable microwave devices *J. Electron. Mater.* **32** 1125–34

[6] Bao P, Jackson T J, Wang X and Lancaster M J 2008 Barium strontium titanate thin film varactors for room-temperature microwave device applications *J. Phys. D: Appl. Phys.* **41** 063001

[7] Pervez N K, Hansen P J and York R A 2004 High tunability barium strontium titanate thin films for RF circuit applications *Appl. Phys. Lett.* **85** 4451–53

[8] Jamil A, Kalkur T S and Cramer C 2007 Tunable ferroelectric capacitor-based voltage controlled oscillator *IEEE Trans. Ultrason. Ferroelectr. Freq. Control* **54** 222–6

[9] Nath J, Ghosh D, Maria J P, Kingon A I, Fathelbab W, Franzon P D and Steer M B 2005 An electronically tunable microstrip bandpass filter using thin-film barium–strontium–titanate (BST) varactors *IEEE Trans. Microw. Theory Technol.* **53** 2707–12

[10] Kim K B and Park C S 2007 Application of RF varactor using $Ba_xSr_{1-x}TiO_3/TiO_2$/HR-Si substrate for reconfigurable radio *IEEE Trans. Utrason. Ferroelectr. Freq. Control* **54** 2227–32

[11] Baniecki J D, Shioga T and Kurihara K 2002 Microstructual and electrical properties of $Ba_xSr_{1-x}Ti_{1+y}O_{3+z}$ thin films prepares by RF magnetron sputtering *Integr. Ferroelectr.* **46** 221–32

[12] Vetelino K, Welsh P, Aguirre M and Abbott B 2004 RF-SAW filter on pyro-suppressed wafers *Proc. IEEE Ultrason. Symp.* pp 449–52

[13] Ogihara M *et al* 2006 LED array integrated with Si driving circuits for LED printer printhead *Electron. Lett.* **42** 881–3

[14] Schelcher G, Brault S, Parrain P, Lefeuvre E, Dufour-Gergam E, Tatoulian M, Bouville D, Desgeorges M, Verjus F and Bosseboeuf A 2011 MEMS process by film transfer using a fluorocarbon anti-adhesive layer *J. Electrochem. Soc.* **158** H545–50

[15] Niklaus F, Kalvesten E and Stemme G 2001 Wafer-level membrane transfer bonding of polycrystalline silicon bolometers for use in infrared focal plane arrays *J. Micromech. Microeng.* **11** 509–13

[16] Guerre R, Drechsler U, Daniel J and Despont M 2008 Low-cost AFM cantilever manufacturing technology *J. Micromech. Microeng.* **18** 115013

[17] Takigawa R, Higurashi E, Suga T and Kawanishi T 2012 Hybrid integration of $LiNbO_3$ thin films on micromachined Si substrates using room-temperature transfer bonding *LTB-3D: Proc 3rd IEEE Int. Workshop Low Temperature Bonding 3D Integration)* p 105

[18] Baron T, Gachon D, Romand J P, Alzuaga S, Ballandras S, Masson J, Catherinot L and Chatras M 2010 A pressure sensor based on a HBAR micromachined structure *FCS: IEEE Int. Frequency Control Symp.* pp 361–4

[19] Hashimoto K, Asano H, Omori T and Yamaguchi M 2004 Ultrawideband surface acoustic wave devices using

Cu-grating/rotated-YX-$LiNbO_3$-substrate structure *Japan. J. Appl. Phys.* **43** 3063–6

[20] Takigawa R, Higurashi E, Suga T and Kawanishi T 2011 Passive alignment and mounting of $LiNbO_3$ waveguide chips on Si substrates by low-temperature solid-state bonding of Au *IEEE J. Sel. Top. Quantum Electron.* **17** 652–8

[21] Kim Y S and Smith R T 1969 Thermal expansion of Lithium Tantalate and Lithium Niobate single crystals *J. Appl. Phys.* **40** 4637–41

[22] Wuu D S, Lin C C, Horng R H, Liao F C and Liu Y H 2001 Etching characteristics and plasma-induced damage of high-k $Ba_{0.5}S_{0.5}TiO_3$ thin-film capacitors *J. Vac. Sci. Technol.* B **19** 2231–6

[23] Shibano T and Oomori T 1997 Sidewall deposition film in platinum etching with Ar/halogen mixed gas plasmas *J. Vac. Sci. Technol.* B **15** 1747–51

[24] Chung C W and Song H G 1997 Study on fence-free platinum etching using chlorine-based gases in inductively coupled plasma *J. Electrochem. Soc.* **144** L294–6

[25] Choi S K, Kim D P, Kim C I and Chang E G 2001 Damage in etching of (Ba,Sr)TiO_3 thin films using inductively coupled plasma *J. Vac. Sci. Technol.* A **19** 1063–7

[26] Abe T, Hong Y G and Esashi M 2003 Highly selective reactive-ion etching using $CO/NH_3/Xe$ gases for microstructuring of Au, Pt, Cu, and 20% Fe–Ni *J. Vac. Sci. Technol.* B **21** 2159